

**Charge Storage Mechanism and Degradation of P2-Type Sodium Transition Metal Oxides in Aqueous Electrolytes**

Journal:	<i>Journal of Materials Chemistry A</i>
Manuscript ID	TA-ART-08-2018-008367.R2
Article Type:	Paper
Date Submitted by the Author:	09-Oct-2018
Complete List of Authors:	Boyd, Shelby; North Carolina State University, Materials Science & Engineering Dhall, Rohan; North Carolina State University, Material Science and Engineering LeBeau, James; North Carolina State University Augustyn, Veronica; North Carolina State University, Materials Science & Engineering

**Charge Storage Mechanism and Degradation of P2-Type Sodium Transition Metal Oxides
in Aqueous Electrolytes**

Shelby Boyd, Rohan Dhall, James M. LeBeau, & Veronica Augustyn *

Department of Materials Science & Engineering

North Carolina State University

Raleigh, NC 27695

*vaugust@ncsu.edu

Abstract

Few transition metal oxides exhibit sufficient stability for aqueous ion intercalation from neutral pH electrolytes for low-cost aqueous Na⁺ batteries and battery-type desalinators. P2 layered Na⁺ manganese-rich oxides have high theoretical capacities and voltages for Na⁺ storage and are extensively investigated for non-aqueous Na⁺ batteries. However, the charge storage mechanism and factors controlling interlayer chemistry and redox behavior of these materials in aqueous electrolytes have not been determined. Here, we take a significant step in establishing their aqueous electrochemical behavior by investigating a series of P2 oxides that exhibit a range of stability in water and ambient air: Na_{0.62}Ni_{0.22}Mn_{0.66}Fe_{0.10}O₂ (NaNMFe), Na_{0.61}Ni_{0.22}Mn_{0.66}Co_{0.10}O₂ (NaNMCo), Na_{0.64}Ni_{0.22}Mn_{0.66}Cu_{0.11}O₂ (NaNMCu), and Na_{0.64}Mn_{0.62}Cu_{0.31}O₂ (NaMCu). Depending on the transition metal composition and potential, all materials exhibit significant irreversible Na⁺ loss during the first anodic cycle followed by water intercalation into the interlayer. The presence of water causes conversion into birnessite-like phases and microscopic exfoliation of the particles. The interlayer affinity for water is primarily driven by the Na⁺ content, which can be tuned by the transition metal composition and the maximum anodic potential during electrochemical cycling. The interlayer water affects the reversible capacity and cycling stability of the oxides, with the highest reversible capacity (~ 40 mAh g⁻¹ delivered in ~ 30 minutes) obtained with NaNMCo. These results present the first studies on the structural effects of aqueous electrochemistry in P2 oxides, highlight the significant differences in the electrochemical behavior of P2 oxides in aqueous vs. non-aqueous electrolytes, and provide guidance on how to use the transition metal chemistry to tune their aqueous charge storage behavior.

I. Introduction

Electrochemical energy storage devices operating in neutral pH electrolytes are attractive because of their low cost and high safety. However, few transition metal oxides exhibit sufficient stability for electrochemical aqueous ion intercalation at neutral pH conditions, as indicated by their Pourbaix diagrams.¹ Among these, layered manganese (Mn) oxides are of interest for aqueous sodium-ion (Na^+) electrochemical energy storage² and battery-type desalination³ due to their redox activity and the abundance and safety of manganese.⁴ The most widely-studied Mn-rich oxides for Na^+ intercalation from aqueous electrolytes are the layered birnessites, $A_x\text{MnO}_2 \cdot n\text{H}_2\text{O}$ (where A represents alkali cations such as Na^+ and Mg^{2+}), with capacities up to 134 mAh g^{-1} .⁵ The complex interlayer of these oxides includes structural water and cations such as sodium, potassium, and magnesium, which makes them relevant for both mono- and multivalent aqueous energy storage devices.^{5,6}

Higher capacities and voltages for Na^+ intercalation have been obtained with P2 layered oxides ($\text{Na}_{0.67}\text{Mn}_{1-x}\text{M}_x\text{O}_2$, where M can be a variety of transition metals like Cu, Co, Fe, etc. and their combinations) in non-aqueous electrolytes, with reversible capacities of 90 - 216 mAh g^{-1} .^{7,8} The P2 terminology developed by Delmas, et al. indicates that the prismatic sites ("P") between the metal oxide layers are occupied by Na^+ and that the layers of edge-sharing transition metal oxide octahedra are arranged in an ...ABBA... stacking sequence ("2"), as depicted in **Figure 1a**.⁹ These materials are of potential interest as high voltage cathodes for aqueous Na^+ batteries and desalinators because they are electrochemically active at anodic potentials within the limited 1.23 V thermodynamic stability window of aqueous electrolytes,^{7,8,10} and have high theoretical capacities, both of which could give rise to high energy density devices. While the intercalation behavior of these materials in non-aqueous electrolytes is fairly well

established,^{7,8,11–20} little is known about their behavior in aqueous electrolytes, where the presence of water is likely to lead to entirely different intercalation phenomena. Recent studies on P2 $\text{Na}_{0.67}\text{Ni}_{0.33}\text{Mn}_{0.67}\text{O}_2$ and $\text{Na}_{0.67}\text{Ni}_{0.25}\text{Mn}_{0.75}\text{O}_2$ in aqueous Na^+ electrolytes showed reversible capacities between 42 – 56 mAh g^{-1} ,^{21,22} but did not provide significant insights into the mechanism, effects of material chemistry on electrochemical behavior, or interlayer affinity for water. In the present work, we perform a systematic study of these fundamental characteristics of P2 oxides and identify the implications for their behavior in aqueous electrolytes.

Water is a unique non-flammable solvent with a higher solvation strength than the standard carbonate-based non-aqueous electrolyte solvents, which leads to higher-conductivity electrolytes.^{23–25} Due to their high polarity and small size, water molecules strongly solvate electrolyte cations such as Na^+ and are expected to co-intercalate into materials upon electrochemical cycling.^{23,26} The possibility of hydronium (H_3O^+) intercalation also needs to be considered in aqueous electrolytes.²⁷ The combination of water and oxygen or carbon dioxide oxidizes and hydrates many P2 layered oxides by spontaneously removing Na^+ and replacing it with water.^{11–13,15,18,28–31} Previous work on P2 oxides cycled in non-aqueous electrolytes has shown that the reactivity to moisture varies with transition metal composition, where $\text{Na}_{0.67}\text{Mn}_{0.66}\text{Ni}_{0.33}\text{O}_2$ is stable in water, but $\text{Na}_{0.6}\text{MnO}_2$, $\text{Na}_{0.67}\text{Mn}_{0.66}\text{Ni}_{0.22}\text{Co}_{0.11}\text{O}_2$, and $\text{Na}_{0.67}\text{Mn}_{0.5}\text{Fe}_{0.5}\text{O}_2$ exhibit spontaneous water and carbonate intercalation upon exposure to water or humid air.^{11,12,18} While the cause of enhanced stability has not been determined, one observed trend is that materials with a superstructure ordering of the transition metals within the oxide layers, such as $\text{Na}_{0.67}\text{Mn}_{0.66}\text{Ni}_{0.33}\text{O}_2$ and $\text{Na}_{0.67}\text{Ni}_{0.33-x}\text{Mn}_{0.66}\text{Cu}_x\text{O}_2$, ($0 \leq x \leq 0.33$) exhibit significantly higher stability in water.^{11,15}

Here, we take a significant step in establishing the effects of transition metal composition on the interlayer affinity for water and aqueous electrochemical behavior of P2 oxides. By synthesizing and characterizing four compositions that exhibit a range of stability in water and ambient air: $\text{Na}_{0.62}\text{Ni}_{0.22}\text{Mn}_{0.66}\text{Fe}_{0.10}\text{O}_2$ (NaNMFe), $\text{Na}_{0.61}\text{Ni}_{0.22}\text{Mn}_{0.66}\text{Co}_{0.10}\text{O}_2$ (NaNMCo), $\text{Na}_{0.64}\text{Ni}_{0.22}\text{Mn}_{0.66}\text{Cu}_{0.11}\text{O}_2$ (NaNMCu), and $\text{Na}_{0.64}\text{Mn}_{0.62}\text{Cu}_{0.31}\text{O}_2$ (NaMCu)^{11,12,15,19} we demonstrate that the transition metal composition affects the affinity of the interlayer for water intercalation and in turn, the electrochemical charge storage behavior. Using structural and electrochemical characterization techniques, we show that these P2 oxides transform to a hydrated birnessite-like phase upon aqueous electrochemical cycling and that the transformation is driven by the redox potential at which a critical amount of Na^+ remains ($\sim 0.4 \text{ Na}^+$ per formula unit) in the interlayer. The phase transformation to a hydrated layered structure is accompanied by significant exfoliation of the layered structures. These results demonstrate that the transition metal composition of layered oxides has a significant effect on the interlayer affinity for water, which in turn affects the structural stability and electrochemical activity in aqueous electrolytes.

II. Methods

II.1 Material Synthesis

The P2 oxides were synthesized by room temperature coprecipitation of transition metal hydroxides and subsequent high-temperature calcination into sodiated transition metal oxides. Specifically, precursor solutions of 0.53 M transition metal acetates [$\text{Mn}(\text{CH}_3\text{COO})_2 \cdot 4\text{H}_2\text{O}$, $\text{Co}(\text{CH}_3\text{COO})_2 \cdot 4\text{H}_2\text{O}$, $\text{Ni}(\text{CH}_3\text{COO})_2 \cdot 4\text{H}_2\text{O}$, $\text{Fe}(\text{CH}_3\text{COO})_2$, and $\text{Cu}(\text{CH}_3\text{COO})_2$, Alfa Aesar] in deionized (DI) water were prepared according to the following molar ratios: (a) 11 : 66 : 22, Co :

Mn : Ni, (b) 11 : 66 : 22, Fe : Mn : Ni, (c) 11 : 66 : 22, Cu : Mn : Ni, and (d) 34 : 66, Cu : Mn. Each solution was added to a 2.25 M aqueous NaOH (Fisher Scientific) solution at ~ 2.5 mL min^{-1} . After precipitation, the hydroxides were washed to $\text{pH} \sim 7$, filtered, dried at 120°C , and ball milled in ethanol with 5 mm spherical zirconia beads (U.S. Stoneware) for 24 hours. The dried ball-milled hydroxides were mixed into an aqueous NaOH solution with 0.704 mol Na^+ per mol of transition metal hydroxide to target a final composition of 0.64 Na^+ . This solution was stirred for 1 hour at room temperature and then at 100°C until dry. The dry powder was annealed in a box furnace (Thermo Scientific) in air at 500°C for 5 hours, cooled to room temperature and ground with a mortar and pestle for 15 minutes before fully calcining at 850°C for 6 hours. All samples were transferred from the furnace while above 100°C to an argon-filled glovebox (MBraun Labstar Pro) with < 0.5 ppm O_2 and H_2O to protect them from the ambient atmosphere, and ground with mortar and pestle for 30 minutes.

II.2 Physical Characterization

The composition of each oxide was analyzed with an inductively-coupled plasma optical emission spectrometer (ICP-OES; Perkin Elmer 8000). 50 mg of each sample was dissolved in aqua regia at 70°C for two hours. All reagents, standards, and samples only contacted polypropylene to avoid accidental leaching of Na from glass. X-ray diffraction (XRD) was performed on an X-ray diffractometer in standard Bragg-Brentano geometry with $\text{Cu-K}\alpha$ radiation (PANalytical Empyrean). Powder samples were rotated at 7.5 RPM, while electrode samples for *ex situ* XRD were stationary. Lattice parameters were determined by Rietveld refinement using the GSAS-II software. **Figure S1** shows the refinement results at higher diffraction angles. The morphology of the electrodes and pristine powders was characterized using a field emission scanning electron microscope (FEI Verios 460L). Reactivity of the as-

synthesized powders upon water exposure was tested by stirring the ground powders in DI water (20 mg mL^{-1}) for 8 days. The excess water was then centrifuged off, and the damp powders were used for XRD, scanning transmission electron microscopy (STEM), and thermogravimetric analysis (TGA).

Samples for STEM were prepared by sonicating the ground pristine powder in ethanol (1 mg mL^{-1}) for 30 minutes, diluting to $150 \text{ }\mu\text{g mL}^{-1}$, and dropcasting $15 \text{ }\mu\text{L}$ onto lacey carbon TEM grids (Pelco) before drying at 100°C in air. Samples of the water-exposed powders were prepared by sonicating in water for 30 minutes, diluting to $200 \text{ }\mu\text{g mL}^{-1}$, and dropcasting $20 \text{ }\mu\text{L}$ onto the lacey carbon TEM grids. These grids were dried overnight at room temperature. The samples were imaged using a probe corrected scanning transmission electron microscope (FEI Titan G2), equipped with a high-brightness field emission gun (X-FEG) and operated at 200 kV . For structural characterization, high-angle annular dark-field (HAADF) images were acquired with a collection inner semi-angle of 77 mrad . The interlayer distances were then directly measured and averaged from several particles. Energy dispersive X-ray spectroscopy (EDS) was used to determine the elemental composition of the synthesized compounds using a FEI Super-X EDS detector with a large solid angle ($\sim 0.7 \text{ sr}$).

TGA was conducted on a SII EXSTAR6000 TG/DTA6200. Dry samples were tested immediately after removal from the glovebox. Water-exposed samples (for 16 days) were first dried for ~ 20 minutes at 50°C , until they formed a slightly damp powder. All samples were tested in aluminum pans between $25 - 300^\circ\text{C}$ using a ramp rate of 5°C min^{-1} in air.

II.3 Electrochemical Characterization

Electrochemistry was conducted in a glass three-electrode 50 mL round bottom flask using a 1 M Na₂SO₄ (Sigma Aldrich) electrolyte, a platinum wire counter electrode (99.997%, Alfa Aesar) and a Ag/AgCl in saturated KCl reference electrode (Pine Instruments). Slurries of active materials were made with 80 wt.% active material, 10 wt.% acetylene black (Alfa Aesar), and 10 wt.% polyvinylidene fluoride (PVDF; Arkema Kynar KV 900) ground together for 5 minutes and stirred overnight in n-methyl pyrrolidone (NMP; Sigma Aldrich) at 990 RPM. An acetylene black slurry was prepared in a similar fashion but without the oxide, containing 67 wt.% acetylene black and 33 wt.% PVDF. Electrodes were made by pasting the slurries onto a ~ 1 cm² area of a 1 x 2 cm titanium mesh (Alfa Aesar) with active material mass loadings of 1 - 3 mg cm⁻², and drying at room temperature for at least 6 hours before drying at 120°C overnight. Ni-plated stainless steel alligator clips were used to hold the working and counter electrodes in the electrolyte. When setting up these aqueous cells, care must be taken to not get the alligator clips wet, or they will rust, increasing the resistance and contaminating the cell. To determine the electrochemical response of all four oxide compositions, cyclic voltammograms (CVs; Bio-Logic MPG-2) were collected at 0.1 mV s⁻¹ between 0 - 0.8 V vs. Ag/AgCl (2.9 - 3.71 V vs. Na/Na⁺). Unless otherwise noted, all potentials referenced in this work are vs. Ag/AgCl. Cycling stability of NaNMCo and NaMCu was characterized at 0.5 mV s⁻¹ for 50 cycles between both 0 - 0.8 V and 0 - 1.1 V. Electrochemical impedance spectroscopy (EIS; Bio-Logic VMP-3) was conducted from 100 mHz to 200 kHz with a 10 mV amplitude at the open circuit potential on the pristine electrodes and after 10 cycles at 0.5 mV s⁻¹. To determine whether the redox potential was affected by a change in electrolyte pH (which would indicate H⁺/H₃O⁺ intercalation), cyclic voltammetry was performed at 1 mV s⁻¹ in Na₂SO₄ electrolytes, with the addition of varying amounts of NaOH to increase the pH. In electrolytes of pH 6, 9, 11, and 13, electrodes were

cycled between 0 - 0.6 V due to the high OER activity in the pH 13 electrolyte. Additionally, electrodes were cycled between 0 – 0.8 V in electrolytes of pH 6, 9 and 11. A pH meter (Mettler Toledo FiveEasy) was used to measure the pH of the electrolytes.

III. Results and Discussion

The aqueous electrochemical behavior of P2 Mn-rich oxides, including the effects of transition metal composition on the electrochemical behavior and interlayer water affinity, was investigated in four oxides (“NaNMFe,” “NaNMCo,” “NaNMCu,” and “NaMCu”) with varying degrees of moisture sensitivity. **Table I** shows the compositions determined by ICP-OES, which verify that the final Na content and *M* ratios were close to the intended composition. Rietveld refinement of the XRD patterns in Figure 1 confirmed that all four compositions formed the expected P2 phase with the hexagonal space group P6₃/mmc. NaNMFe, NaNMCo, and NaNMCu were refined as a single phase, while NaMCu was refined as 89.7 wt% P2 with 10.3 wt% CuO. Results from the refinement, also in Table 1, show little variation in lattice parameters with changes in transition metal composition. There is ~ 1% change in the *a*-lattice parameter between NaNMCo and the other compositions, but this value is in agreement with the reported refinement results.³² The ICP-OES results and the similar *c* lattice parameters indicate that all compositions contain about the same amount of Na⁺ in the as-synthesized condition. The XRD results also show that the NaNMCu and NaMCu exhibited two superlattice ordering peaks at 27.25 and 28.47 °,^{15,33} which were not included in the Rietveld refinement. The larger ionic radii of Ni²⁺ and Cu²⁺, as compared to Mn³⁺ and Mn⁴⁺, promote formation of a $\sqrt{3}a \times \sqrt{3}a$ hexagonal superlattice, especially in compositions with a 2 : 1 ratio of Mn : Cu, Ni, or Ni and Cu,^{15,33,34}

which leads to Na⁺/vacancy ordering.³⁵ The similar radii of Co³⁺, Fe³⁺, Mn³⁺, and Mn⁴⁺ allow random cation mixing and disrupt this ordering.^{33,34}

Table I. Composition (from ICP-OES) and lattice parameters (from Rietveld refinement) of the P2-type Na_{0.6}Mn_{0.66}M_{0.34}O₂.

Material	Composition	a (Å)	c (Å)	Rwp	GOF
NaNMFe	Na _{0.62} Ni _{0.21} Mn _{0.62} Fe _{0.10} O ₂	2.893487	11.188151	4.681	3.47
NaNMCo	Na _{0.61} Ni _{0.21} Mn _{0.62} Co _{0.10} O ₂	2.864602	11.200887	5.572	4.18
NaNMCu	Na _{0.64} Ni _{0.22} Mn _{0.66} Cu _{0.12} O ₂	2.891256	11.15571	4.663	2.84
NaMCu	Na _{0.64} Mn _{0.62} Cu _{0.31} O ₂	2.89903	11.17451	4.68	2.65

Rwp: weighted profile R-factor; GOF: goodness of fit

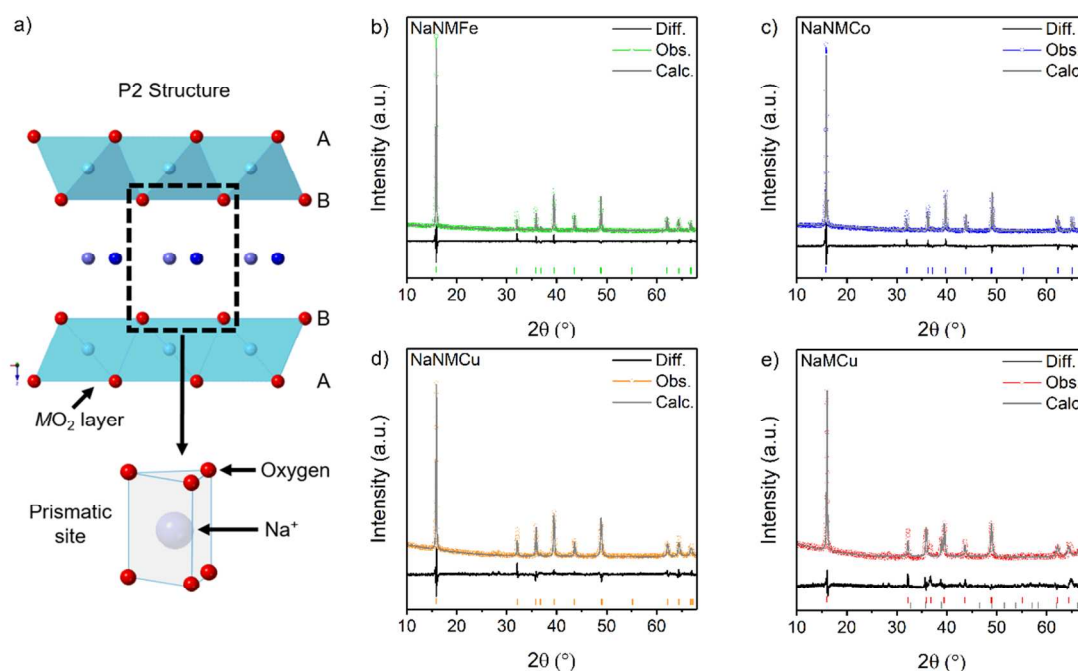


Figure 1. Structure of as-synthesized materials: a) schematic illustrating the P2 structure with alternating MO_2 (where M is 0.64 Mn and 0.34 Cu or 0.22 Ni and 0.11 Fe, Co, or Cu) layers of edge-sharing octahedra and interlayer Na^+ . The refined XRD patterns show that each of the four compositions crystallizes into this structure: b) NaNMFe, c) NaNMCo, d) NaNMCu, and e) NaMCu. The colored tick marks show the location of the P2 peaks in each graph. The gray tick marks in e) show the CuO peaks.

As shown by the SEM images of pristine electrodes in **Figure S2**, all four materials have similar sub-micron primary particles, with larger, micron-size secondary particle aggregates throughout. The faceted crystals of the active materials show the hexagonal basis of this crystal structure. To further characterize the structure and composition, HAADF-STEM imaging and corresponding EDS elemental mapping were performed on a particle of NaNMCo. **Figure 2a** shows that in agreement with the XRD results, the material crystallizes in a layered structure. The interlayer spacing, as measured from the HAADF-STEM image, is ~ 5.8 Å. The composition maps for each individual element in NaNMCo (**Figure 2b-f**), and a composite EDS map of Na and Mn (**Figure 2g**) demonstrate that as expected, the transition metals reside within the metal oxide layers, while the Na^+ resides in the interlayer.

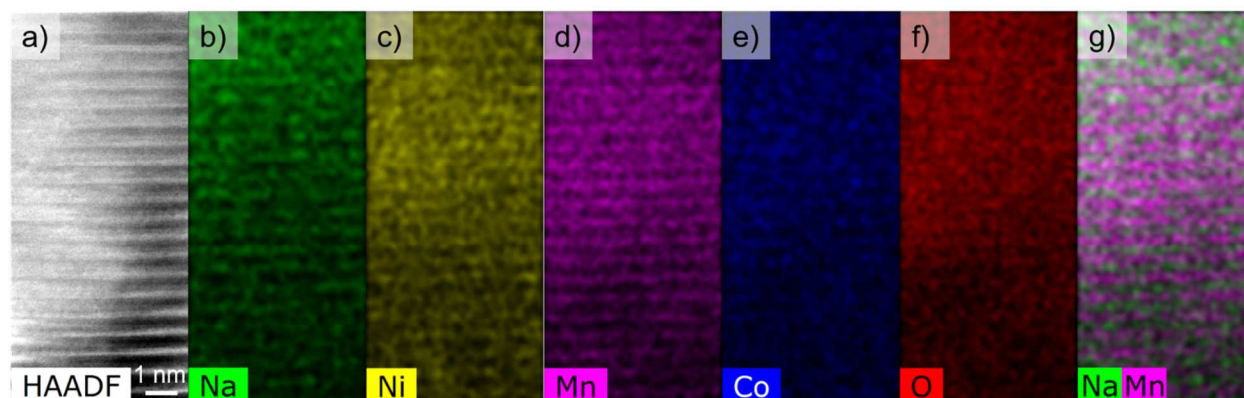


Figure 2. Structure and composition of an individual particle of NaNMCo: a) HAADF-STEM image showing the layered structure with an average interlayer spacing of 5.8 Å; corresponding EDS elemental mapping of b) Na, c) Ni, d) Mn, e) Co, and f) O; g) composite EDS elemental mapping of Na and Mn, which shows that Na is located between layers of Mn.

Role of Transition Metal Composition on the Interlayer Affinity for Water

Water stability tests and aqueous electrochemistry were conducted to determine the mechanism of aqueous charge intercalation into P2 oxides as a function of transition metal composition. First, XRD and HAADF-STEM were used to understand the local structure of each composition before and after exposure to DI water for 8 days. The XRD data (**Figure 3**) shows that after water exposure, both the NaNMFe and NaNMCo exhibit a partial transformation to a phase with a larger interlayer spacing of ~ 7 Å as indicated by the emergence of a new peak at $\sim 12.5^\circ$. This is accompanied by a loss of Na^+ , shown by the decrease in the position of the P2 (002) peak at $\sim 16^\circ$.^{16,17,32} No phase transformation was detected in NaNMCu or NaMCu. The presence of a new phase with a larger interlayer spacing of ~ 7 Å in NaNMFe and NaNMCo implies the transformation into a hydrated, birnessite-like structure, which has been reported for

P2 materials without superstructure ordering.¹¹ P2 Na_xMnO_2 and $\text{Na}_x\text{Ni}_{0.22}\text{Co}_{0.11}\text{Mn}_{0.66}\text{O}_2$ desodiated to $x < 0.35$ Na^+ in non-aqueous electrolytes spontaneously intercalate water into the half-empty Na^+ sites and form a phase with larger interlayer spacing when exposed to air.^{11,18,19} A similar mechanism is likely to occur in the water-exposed NaNMCu and NaNMFe.

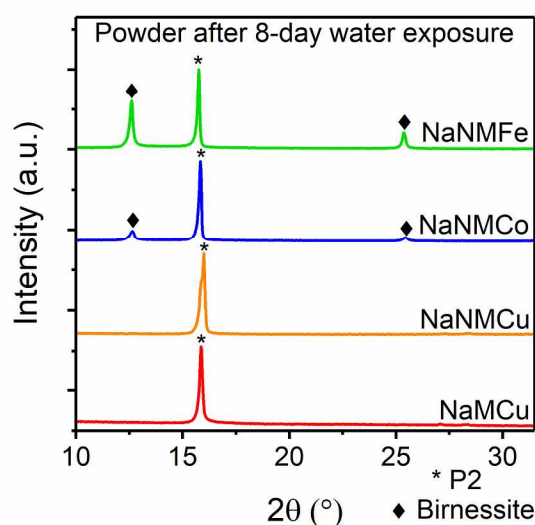


Figure 3. *Ex situ* XRD of the four compositions of P2 oxides after water exposure for 8 days, showing that the NaNMFe and NaNMCo form a birnessite-like phase (♦) in addition to the P2 phase (*). Both NaNMCu and NaMCu retain the P2 phase, indicating improved stability in the presence of water as compared to NaNMFe and NaNMCo.

While XRD measures the average structural change, STEM provides a local measure of the effect of water exposure on the material structure, particularly the interlayer uniformity, lending insight into how transition metal composition affects interlayer chemistry in layered Na^+ transition metal oxides. **Figure 4** shows the STEM images of the layered structure for all four

compositions before and after water exposure. The interlayer spacings measured with XRD and STEM on powders, and XRD on electrodes after aqueous electrochemistry, are listed in **Table II**. Raw data from the STEM measurements is listed in **Table S1**. The pristine NaNMFe in **Figure 4a** exhibits an irregular interlayer spacing, while the pristine NaNMCo, NaNMCu, and NaMCu (**Figure 4c, e, and g**) all appear uniform with an average interlayer spacing $\sim 5.8 - 5.9 \text{ \AA}$. This uniformity is expected, as care was taken to protect the “pristine” samples from air exposure after synthesis. The irregular layers in **Figure 4a** show that the NaNMFe is the most reactive composition, and had already begun reacting with the atmosphere to form a partially hydrated structure. **Figure 4b, d, f, and h** show the water-exposed NaNMFe, NaNMCo, NaNMCu, and NaMCu, respectively. The NaNMFe after water exposure has an increased average interlayer spacing of 6.16 \AA , closer to the hydrated spacing of birnessite. The washed NaNMFe in **Figure 4b** appears more uniform than the pristine material, which could be due to more complete water intercalation into the interlayer, or because the area imaged on the water-exposed sample was thicker than on the pristine samples. After water exposure, NaNMCo (**Figure 4d**) exhibits turbostratic layering, which is indicated by the large standard deviation in the interlayer spacing measurement although the average value remains close to the pristine NaNMCo. After water exposure, the NaNMCu and NaMCu appear uniform and do not exhibit a significant change in the interlayer spacing as compared to the pristine material.

Table II. Interlayer spacing of the four compositions of P2 oxides measured with XRD and STEM for pristine, water-exposed, and electrochemically cycled samples.

Material	Pristine interlayer spacing (\AA)	Interlayer spacing after water exposure (\AA)	Interlayer spacing after electrochemical cycling
----------	--	--	--

	XRD	STEM	XRD	STEM	(Å) XRD
NaNMFe	5.60	5.39 ± 1.00	5.62; 7.02	6.16 ± 0.59	5.67; 7.08
NaNMCo	5.62	5.78 ± 0.23	5.60; 7.00	5.67 ± 1.62	5.69; 7.08
NaNMCu	5.58	5.77 ± 0.14	5.56	5.29 ± 0.35	5.66; 7.02
NaMCu	5.58	5.90 ± 0.14	5.58	5.57 ± 0.52	5.58

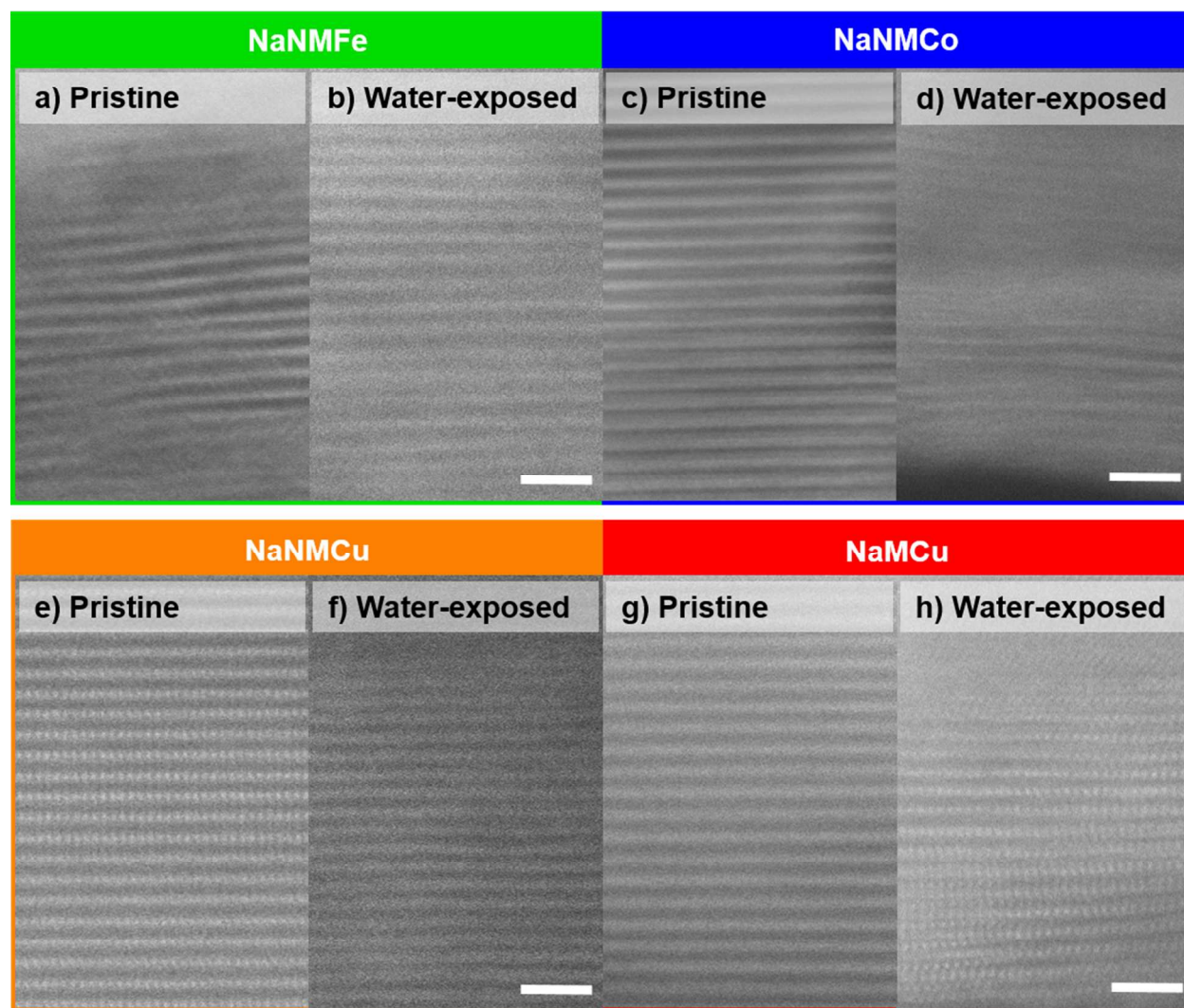


Figure 4. STEM images of the layered structure of the four compositions of P2 oxides before (a, c, e, g) and after (b, d, f, h) water exposure (scale bar = 2 nm) indicate that the NaNMFe and

NaNMCo experience an increase in interlayer spacing with water exposure along with more interlayer spacing disorder, while NaNMCu and NaMCu retain the same interlayer spacing.

TGA was performed on each composition before and after water exposure to further characterize the effect of water intercalation into the interlayer (**Figure S3**). The pristine materials exhibit a small amount of mass loss from water adsorption following their short (~30 minute) exposure to ambient air. After water exposure, all four compositions exhibit increased mass loss between ~ 70 and 300°C that is due to the loss of both surface and interlayer water. The amount of water lost from NaNMFe and NaNMCo is significantly greater than that lost from NaNMCu and NaMCu, which correlates well with the variation in interlayer spacing before and after water exposure measured with XRD and STEM. Given the lack of interlayer spacing change in NaMCu from XRD and STEM, the mass loss from water-exposed NaMCu (~ 0.13 mol of H₂O) is likely entirely due to adsorbed surface water. Also, given that the surface area, morphology, and hydrophilicity of each of the four compositions is similar, it can be assumed that all four materials exhibit similar amounts of surface-adsorbed water. With these assumptions and the TGA results, the compositions after water exposure are: NaNMFe·0.32H₂O, NaNMCo·0.44H₂O, NaNMCu, and NaMCu, where the amount of water indicates structural water in the interlayer. Overall, both local and average structural characterization techniques demonstrate that the reactivity of layered oxides with water decreases when copper is substituted into the transition metal layer, consistent with prior studies.^{15,36–38}

The XRD, ICP-OES, SEM, and STEM results indicate that the as-synthesized materials of each composition are iso-structural, have similar Na⁺ content, and exhibit similar morphologies. This permits the exploration of the effect of transition metal composition on the materials'

electrochemical activity in a neutral-pH aqueous Na^+ electrolyte. Each composition was electrochemically cycled in a 1 M Na_2SO_4 electrolyte, which has a pH of ~ 6 . **Figure 5** shows the first and second CVs of each composition between 0 – 0.8 V at 0.1 mV s^{-1} . All four P2 oxides exhibit electrochemical activity in this potential range, but in contrast to their similar structures and morphologies, each composition exhibits a unique electrochemical response. The first anodic cycle of all four compositions shows redox peaks, with a subsequent decrease in capacity and peak definition depending on composition. NaNMFe exhibits poorly-defined redox peaks and a semi-rectangular CV even in the first cycle, with no distinct peaks in the second cycle. NaNMCo exhibits defined redox peaks in the first cycle, but adopts a more rectangular, capacitive CV after the first cycle. NaNMCu exhibits more defined redox peaks than NaNMCo , and retains these peaks and a slightly higher capacity in the second cycle. NaMCu exhibits well-defined redox peaks in both the first and second cycle. This is a significant difference from the non-aqueous CVs of these P2 oxides, which typically exhibit defined redox peaks and little capacitive background.^{7,8,15,32} The development of more capacitive CVs is indicative of the lack of well-defined potentials for ion intercalation into the interlayer, which is similar to the electrochemical behavior of hydrated birnessite.^{27,28,39} **Table III** shows the capacities and Coulombic efficiencies (CE) for the first and second cycles of all four materials. The most water-sensitive compositions, NaNMFe and NaNMCo , show the highest 1st cycle capacities and highest CEs, indicating irreversible Na^+ deintercalation during the first anodic sweep. The more water-stable materials exhibit more reversible electrochemistry with lower 1st cycle capacities and CEs nearer to 1. It should be noted that the redox potentials were not affected by change of electrolyte pH (**Figure S4** and **S5**), which indicates that the intercalation mechanism is likely primarily due to Na^+ intercalation and not H_3O^+ .^{27,40,41}

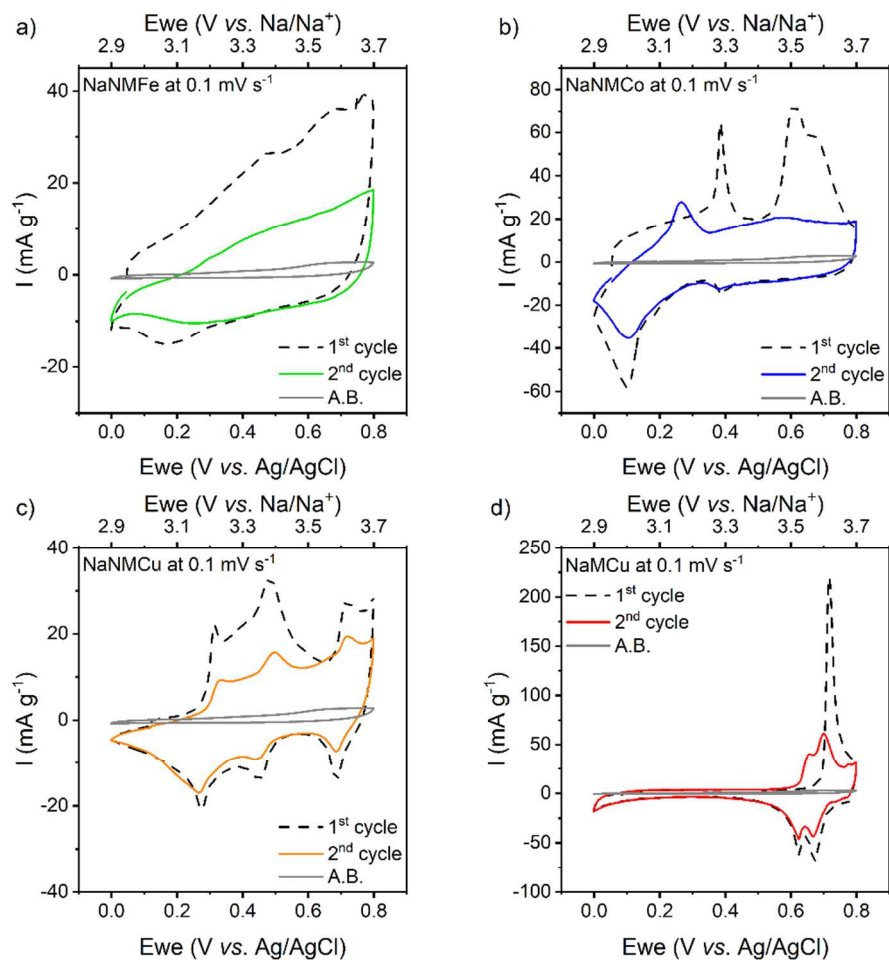


Figure 5. Electrochemistry of the four compositions of P2 oxides in an aqueous Na^+ electrolyte at 0.1 mV s^{-1} : a) NaNMFe exhibits a semi-rectangular CV even in the first cycle, b) NaNMCo exhibits defined redox peaks in the first cycle and an almost rectangular CV in the second, c) NaNMCu retains most of its redox peaks during the second cycle, indicating higher retention of the P2 phase, and d) NaMCu also retains most of its redox peaks and thus the P2 structure. “A.B” represents an acetylene black electrode on Ti mesh; it demonstrates that the measured current is primarily from the redox activity of the transition metal oxide particles in the electrode.

Table III. Anodic capacities and Coulombic efficiencies of the four compositions of P2 oxides in 1 M aqueous Na₂SO₄ electrolyte cycled at 0.1 mV s⁻¹.

Material	1 st cycle anodic capacity (mAh g ⁻¹)	1 st cycle CE	2 nd cycle anodic capacity (mAh g ⁻¹)	2 nd cycle CE	Initial Na ⁺ content	Na ⁺ remaining after 1 st anodic cycle
NaNMFe	47.7	2.30	16.6	0.90	0.62	0.39
NaNMCo	60.9	1.54	31.9	0.95	0.61	0.44
NaNMCu	32.0	1.58	19.5	1.11	0.64	0.52
NaMCu	30.4	0.99	24.9	0.97	0.64	0.52

The water exposure results and the varied electrochemical behavior of these four compositions indicate that their structural response to electrochemical cycling in aqueous electrolytes is not uniform. To investigate the intercalation mechanism in aqueous electrolytes in this class of materials, *ex situ* XRD of the electrodes was performed before and after cycling at 0.1 mV s⁻¹ in 1 M Na₂SO₄ electrolyte to determine the structural implications of aqueous electrochemistry (**Figure 6**). Both NaNMFe and NaNMCo transform almost entirely to a phase with a larger interlayer spacing of ~ 7 Å. While the formation of such a birnessite-like phase was observed upon exposure to water (**Figure 3**), it is clear that electrochemical cycling leads to even more water intercalation into the structure. NaNMCu partially transforms, and exhibits a two-phase structure after cycling with some retained P2 phase, while NaMCu remains completely in the P2 structure. These results indicate that electrochemical cycling leads to further water intercalation into P2 oxides, but that this reactivity can be decreased by the substitution of copper into the transition metal oxide layer.

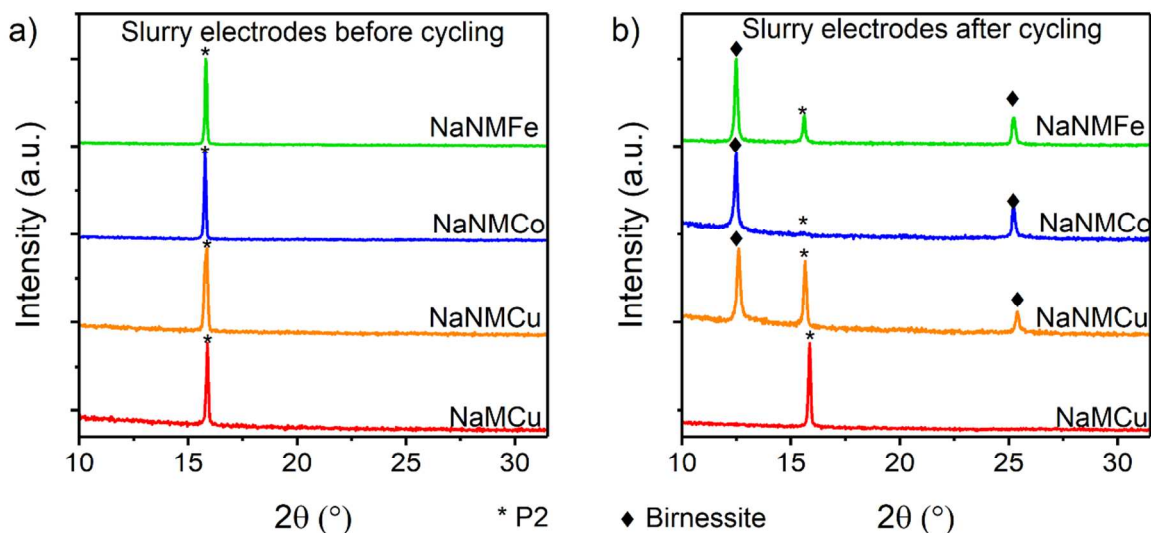


Figure 6. *Ex situ* XRD of slurry electrodes before (a) and after (b) electrochemical cycling in 1 M Na₂SO₄ aqueous electrolyte. a) Before electrochemical cycling, the (002) peak of the P2 phase is at the same position for all compositions indicating similar Na⁺ content and interlayer spacing. b) After electrochemical cycling, NaNMFe and NaNMCu almost completely transform to a birnessite-like phase. NaNMCu partially transforms, while NaMCu retains the P2 phase and the highest final Na⁺ content, as indicated by the slightly higher position of the (002) peak at ~ 17

o 16

According to the initial composition of each material in **Table III**, and assuming no parasitic reactions or H⁺ or H₃O⁺ co-intercalation, the Na⁺ content after the first anodic cycle is 0.44 for NaNMFe, 0.39 for NaNMCo, 0.52 for NaNMCu, and 0.52 for NaMCu. NaNMCo is the only material to be electrochemically oxidized to a Na⁺ content close to 0.35 Na⁺. However, Na⁺ is spontaneously extracted from these materials upon atmospheric or water exposure,¹² so the actual final Na⁺ content is likely lower than predicted by the first anodic capacity. When cycled in non-aqueous electrolytes, the average redox potential of P2 oxides increases with substitution

of a first row transition metal of increasing atomic number, from Fe to Cu.^{32,37,42} This higher redox potential means less Na^+ can be extracted between 0 – 0.8 V, which causes the decreased water intercalation during electrochemical cycling and the lower capacity of the Cu-substituted materials. The increased Na^+ content stabilizes the material interlayer and reduces its affinity for water. According to this hypothesis, the NaMCu does not transform to a birnessite-like phase because its higher redox potential limits Na^+ extraction in the aqueous electrolyte.

Effect of Potential Window on the Interlayer Affinity for Water of P2 Oxides in Aqueous Electrolytes

To test the hypothesis that the Na^+ content remaining in the interlayer determines the interlayer affinity for water in P2 oxides cycled in aqueous electrolytes, NaNMCo and NaMCu were cycled between 0 – 0.8 V and 0 – 1.1 V (2.9 – 3.7 and 4.0 V vs. Na/Na⁺). These compositions were chosen because NaNMCo shows a phase transformation with water exposure and NaMCu showed no reactivity over the more narrow 0 – 0.8 V potential window. **Figure S6** shows the CVs of both compositions over each potential window at 0.5 mV s⁻¹. The additional 0.3 V does not alter the CV of NaNMCo (**Figure S6a** and **b**). However, the CVs of NaMCu cycled to 1.1 V (**Figure S6d**) shows the first cycle loss of redox peaks. **Figure 7a** shows that the increase in anodic potential increases the first cycle anodic capacity from 65 to 83 mAh g⁻¹ for NaNMCo, and from 29 to 60 mAh g⁻¹ for NaMCu. The 0.5 mV s⁻¹ sweep rate used for the cycling stability tests correlates to a 2.27C rate in a galvanostatic cycling experiment. At a ~ 2C rate in non-aqueous electrolytes over a ~ 1.5 – 2 V wide potential window, the capacities of these P2 oxides are 88 mAh g⁻¹ for NaNMCo⁴³ and ~ 45 mAh g⁻¹ for NaMCu.³⁷ These values indicate that in the first anodic cycle, the electrochemical behavior of the P2 oxides in aqueous

electrolytes is similar to the non-aqueous electrolytes and that there is good utilization of the active material. **Figure 7b** shows that both NaNMCo and NaMCu cycled to 1.1 V experienced large irreversible anodic capacity loss in the first cycle. After 50 cycles at 0.5 mV/s, the XRD patterns (**Figure 7c**) show formation of a birnessite phase in both NaNMCo and NaMCu cycled to 1.1 V. This supports the hypothesis that the interlayer affinity for water is due to the amount of Na^+ remaining in the interlayer as determined by the redox potential of the transition metals in the oxide, which is conceptualized in **Figure 8**. The broad XRD peak in the NaNMCo electrodes at $\sim 18^\circ$ was attributed to a contracted interlayer spacing observed at low Na^+ content when cycling in non-aqueous electrolytes,^{37,44–47} and the new peak at $\sim 24.5^\circ$ may also result from the increasingly disordered structure.

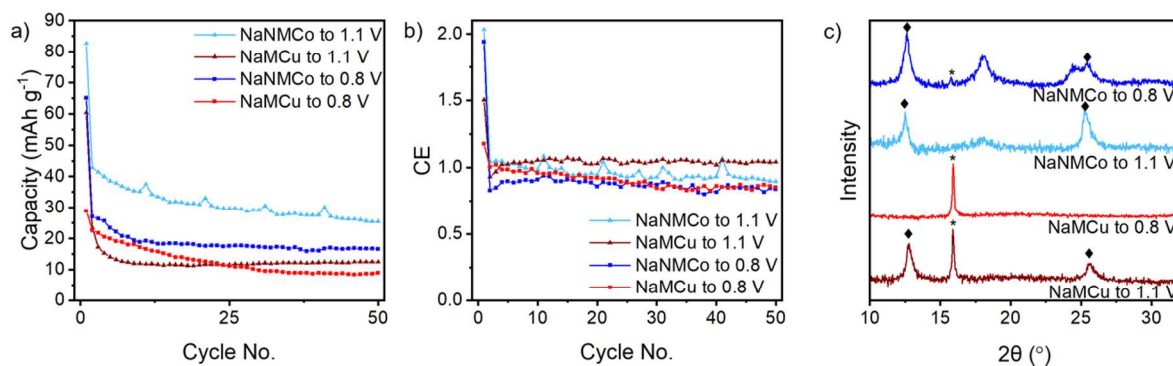


Figure 7. Cycling stability of NaNMCo and NaMCu at 0.5 mV s^{-1} in $1 \text{ M Na}_2\text{SO}_4$ over two different potential windows. a) Anodic capacity, b) Coulombic efficiency, and c) *ex situ* XRD of the electrodes after 50 cycles at 0.5 mV s^{-1} . * indicates the P2 phase, while ♦ indicates the birnessite phase.

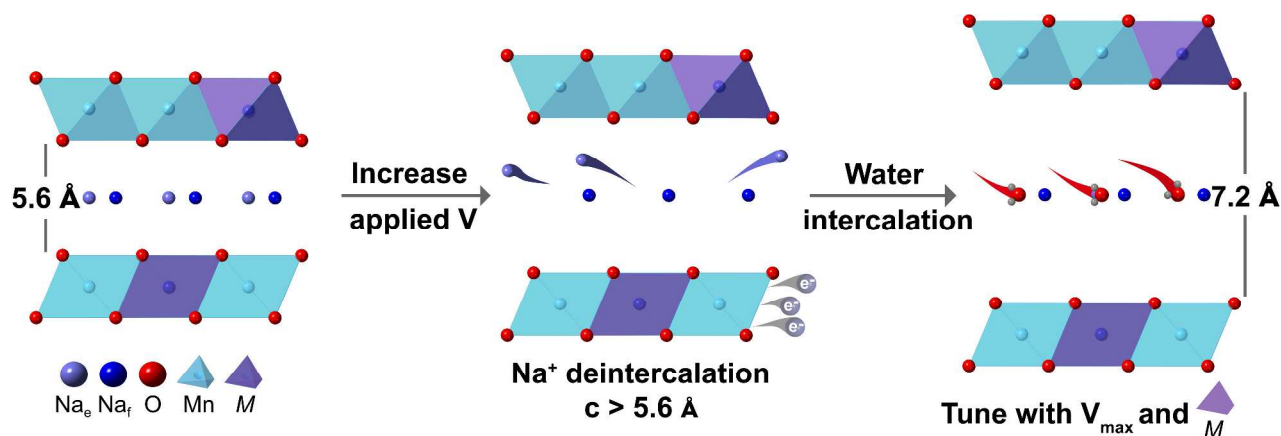


Figure 8. Schematic of the transformation from a P2 oxide to a birnessite-type oxide with Na⁺ deintercalation in aqueous electrolytes. The electrostatic repulsion between facing oxygen anions increases the interlayer spacing of the P2 oxide with Na⁺ deintercalation. At a certain amount of Na⁺ in the interlayer (~ 0.4 Na⁺ per formula unit), which can be controlled by the transition metal *M* content and the applied maximum anodic potential V_{\max} , water is intercalated into the interlayer, transforming the structure to a birnessite-like phase.

The structural transformation into a birnessite phase also led to significant particle damage. SEM images of NaNMCo and NaMCu before and after cycling to 0.8 and 1.1 V in **Figure 9** show that the intercalation of water severely exfoliates and damages the oxides. This same damage occurred in NaNMCo after water exposure (and no electrochemical cycling) (**Figure S7**). The NaMCu cycled to 0.8 V, which did not show a birnessite phase transition, did not have this same degree of damage. EIS was used to characterize the impedance of the electrodes after electrochemical cycling to 0.8 V. The results were modeled with an equivalent circuit (as described in the SI, **Figure S8**) to quantify the changes in the charge transfer resistance and diffusion coefficient. The capacity decline of the NaMCu cycled to 0.8 V is likely due to an

increase in the charge transfer resistance (**Table S3**). The mechanism of capacity fade in NaMCu cycled to 0.8 V is likely similar to its behavior in non-aqueous electrolytes, which showed no significant changes in the XRD patterns before and after cycling even though there was a systematic decrease of redox peak intensities during electrochemical cycling.³⁷ While cycling to 1.1 V improved the capacity of NaMCu, the EIS results showed a large increase in the charge transfer resistance after the first 10 cycles (**Figure S9**). In the case of NaNMCo, which transformed to a birnessite phase and had significant particle exfoliation, **Table S3** shows that the diffusion coefficient decreased and the charge transfer resistance increased after the first 10 cycles. This suggests that Na⁺ diffusion within the NaNMCo was impeded either by the structural disorder after water intercalation, or by the interlayer water itself. While the water may act as a diffusion barrier, the particle damage from water intercalation shown in **Figure 9b, c, and f** indicates that particle exfoliation and fracture also contributed to the rise in impedance, and especially charge transfer resistance, after cycling.

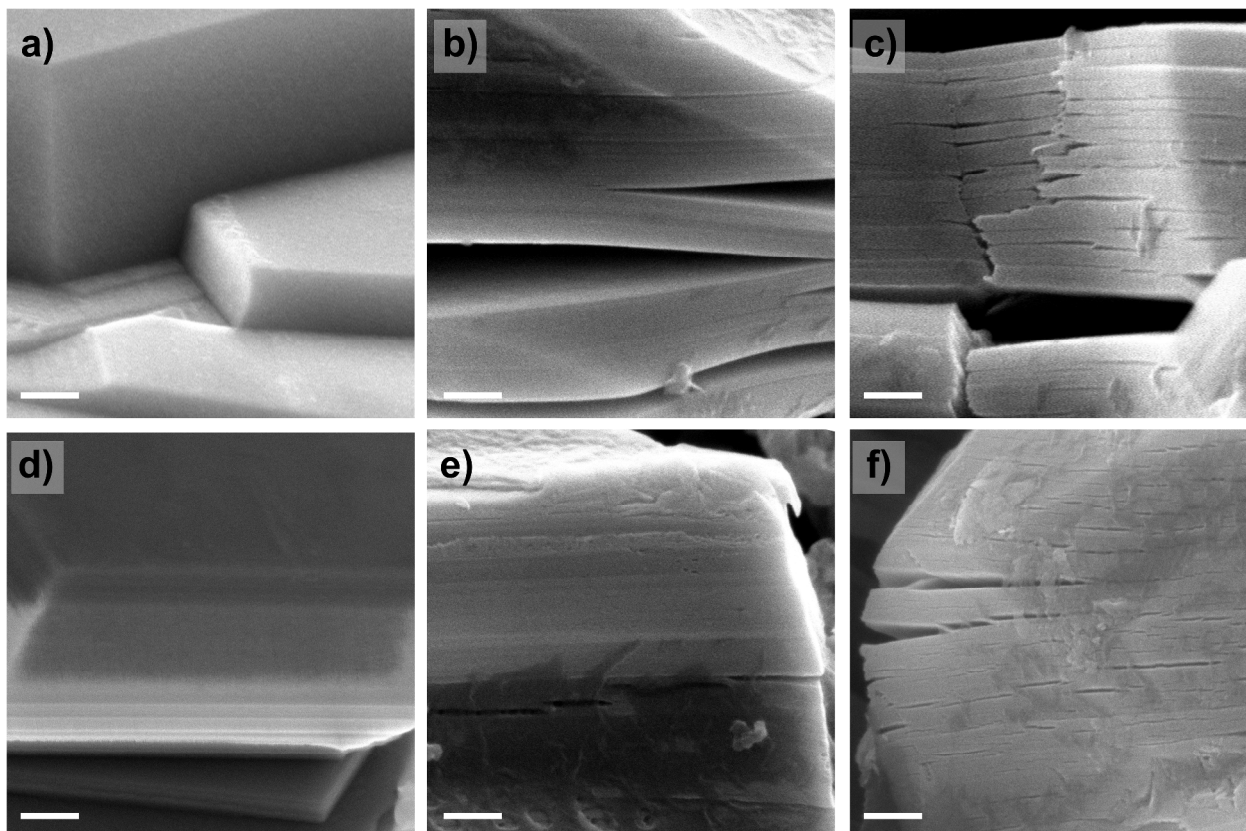


Figure 9. SEM images showing the microstructural effects of water intercalation in P2 oxides. a) Pristine NaNMCo, b) NaNMCo after 50 cycles to 0.8 V, c) NaNMCo after 50 cycles to 1.1 V, d) pristine NaMCu, e) NaMCu after 50 cycles to 0.8 V, and f) NaMCu after 50 cycles to 1.1 V. The water intercalation and transformation to a birnessite phase cause large sections of the particles to delaminate, and even fracture. All materials exhibited an increase in surface roughness with cycling, but NaMCu showed very little exfoliation after cycling to 0.8 V. 100 nm scale bar.

IV. Conclusions

This study establishes the interlayer chemistry and charge storage mechanism of P2 layered Na^+ oxides in aqueous electrolytes. At a critical interlayer Na^+ content ($\sim 0.4 \text{ Na}^+$ per formula unit), water intercalates into the materials which leads to formation of a birnessite-like layered

structure and severe exfoliation of the particles. The potential at which the critical Na^+ content is reached is controlled by the redox potential of the oxides, which is in turn determined by the transition metal composition. While these P2 oxides experience a large capacity loss due to the transformation to a birnessite-like phase, their first cycle capacities are comparable to those obtained with non-aqueous electrolytes. Decreasing the particle size of the P2 oxides may enable higher capacity retention by allowing the particles to expand and contract more uniformly during cycling, while maintaining good contact within the composite electrode. Additionally, this type of electrochemically-induced exfoliation process may be useful for synthesis of nanosheets of these materials. Overall, this work provides fundamental understanding of the effects of the transition metal composition on the aqueous interlayer chemistry and electrochemical activity of manganese-rich P2 layered Na^+ oxides, which are of interest for aqueous Na^+ energy storage and desalination applications.

V. Conflicts of Interest

There are no conflicts of interest to declare.

VI. Acknowledgements

The authors thank Ruocun (John) Wang for assistance with TGA. This material is based upon work supported by the National Science Foundation Graduate Research Fellowship Program under Grant No. 571800 (to S. B.). V.A. acknowledges start-up funding support from North Carolina State University and the University Global Partnership Network. This work was performed in part at the Analytical Instrumentation Facility (AIF) at North Carolina State

University, which is supported by the State of North Carolina and the National Science Foundation (award number ECCS-1542015). The AIF is a member of the North Carolina Research Triangle Nanotechnology Network (RTNN), a site in the National Nanotechnology Coordinated Infrastructure (NNCI).

VII. References

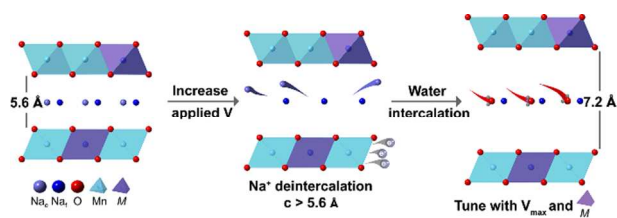
- 1 S. Boyd and V. Augustyn, *Inorg. Chem. Front.*, 2018, **5**, 999–1015.
- 2 H. Kim, J. Hong, K. Y. Park, H. Kim, S. W. Kim and K. Kang, *Chem. Rev.*, 2014, **114**, 11788–11827.
- 3 M. E. Suss and V. Presser, *Joule*, 2018, **2**, 10–15.
- 4 C. P. Grey and J. M. Tarascon, *Nat. Mater.*, 2016, **16**, 45–56.
- 5 M. Feng, Q. Du, L. Su, G. Zhang, G. Wang, Z. Ma, W. Gao, X. Qin and G. Shao, *Sci. Rep.*, 2017, **7**, 2219.
- 6 X. Sun, V. Duffort, B. L. Mehdi, N. D. Browning and L. F. Nazar, *Chem. Mater.*, 2016, **28**, 534–542.
- 7 W. Kang, D. Y. W. Yu, P.-K. K. Lee, Z. Zhang, H. Bian, W. Li, T.-W. W. Ng, W. Zhang and C.-S. Lee, *ACS Appl. Mater. Interfaces*, 2016, **8**, 31661–31668.
- 8 G. Venkatesh, B. Kishore, R. Viswanatha, D. Aurbach and N. Munichandraiah, *J. Electrochem. Soc.*, 2017, **164**, A2176–A2182.
- 9 C. Delmas, C. Fouassier and P. Hagenmuller, *Phys. B+C*, 1980, **99**, 81–85.

- 10 M. Pourbaix, National Association of Corrosion Engineers, Houston, Tx, Second., 1974, pp. 234–286.
- 11 Z. Lu and J. R. Dahn, *Chem. Mater.*, 2001, **13**, 1252–1257.
- 12 V. Duffort, E. Talaie, R. Black and L. F. Nazar, *Chem. Mater.*, 2015, **27**, 2515–2524.
- 13 M. H. Han, N. Sharma, E. Gonzalo, J. C. Pramudita, H. E. A. Brand, J. M. López del Amo and T. Rojo, *J. Mater. Chem. A*, 2016, **4**, 18963–18975.
- 14 E. De La Llave, E. Talaie, E. Levi, P. K. Nayak, M. Dixit, P. T. Rao, P. Hartmann, F. Chesneau, D. T. Major, M. Greenstein, D. Aurbach and L. F. Nazar, *Chem. Mater.*, 2016, **28**, 9064–9076.
- 15 L. Zheng, J. Li and M. N. Obrovac, *Chem. Mater.*, 2017, **29**, 1623–1631.
- 16 Z. Lu and J. R. Dahn, *J. Electrochem. Soc.*, 2001, **148**, A1225–A1229.
- 17 D. H. Lee, J. Xu and Y. S. Meng, *Phys. Chem. Chem. Phys.*, 2013, **15**, 3304–3312.
- 18 A. Caballero, L. Hernán, J. Morales, L. Sánchez, J. Santos Peña and M. A. G. Aranda, *J. Mater. Chem.*, 2002, **12**, 1142–1147.
- 19 D. Buchholz, L. G. Chagas, C. Vaalma, L. Wu and S. Passerini, *J. Mater. Chem. A*, 2014, **2**, 13415–13421.
- 20 R. J. Clément, P. G. Bruce and C. P. Grey, *J. Electrochem. Soc.*, 2015, **162**, A2589–A2604.
- 21 Y. Zhang, K. Ye, K. Cheng, G. Wang and D. Cao, *Electrochim. Acta*, 2014, **148**, 195–202.

- 22 F. Yu, S. Zhang, C. Fang, Y. Liu, S. He, J. Xia, J. Yang and N. Zhang, *Ceram. Int.*, 2017, **43**, 9960–9967.
- 23 O. Borodin, L. Suo, M. Gobet, X. Ren, F. Wang, A. Faraone, J. Peng, M. Olguin, M. Schroeder, M. S. Ding, E. Gobrogge, A. von Wald Cresce, S. Munoz, J. A. Dura, S. Greenbaum, C. Wang and K. Xu, *ACS Nano*, 2017, **11**, 10462–10471.
- 24 W. Wu, S. Shabhag, J. Chang, A. Rutt and J. F. Whitacre, *J. Electrochem. Soc.*, 2015, **162**, A803–A808.
- 25 L. Suo, O. Borodin, Y. Wang, X. Rong, W. Sun, X. Fan, S. Xu, M. A. Schroeder, A. V. Cresce, F. Wang, C. Yang, Y.-S. Hu, K. Xu and C. Wang, *Adv. Energy Mater.*, 2017, **7**, 1701189.
- 26 B. W. Byles, D. A. Cullen, K. L. More and E. Pomerantseva, *Nano Energy*, 2018, **44**, 476–488.
- 27 S.-L. Kuo and N.-L. Wu, *J. Electrochem. Soc.*, 2006, **153**, A1317–A1324.
- 28 Y. Li, X. Feng, S. Cui, Q. Shi, L. Mi and W. Chen, *CrystEngComm*, 2016, **18**, 3136–3141.
- 29 K. S. Abou-El-Sherbini, M. H. Askar and R. Schöllhorn, *Solid State Ionics*, 2002, **150**, 407–415.
- 30 T. A. Eriksson, Y. J. Lee, J. Hollingsworth, J. A. Reimer, E. J. Cairns, X. F. Zhang and M. M. Doeff, *Chem. Mater.*, 2003, **15**, 4456–4463.
- 31 M. H. Han, E. Gonzalo, N. Sharma, J. M. López Del Amo, M. Armand, M. Avdeev, J. J. Saiz Garitaonandia and T. Rojo, *Chem. Mater.*, 2016, **28**, 106–116.
- 32 D. Buchholz, A. Moretti, R. Kloepsch, S. Nowak, V. Siozios, M. Winter and S. Passerini,

- Chem. Mater.*, 2013, **25**, 142–148.
- 33 Z. Lu, R. A. Donaberger and J. R. Dahn, *Chem. Mater.*, 2000, **12**, 3583–3590.
- 34 R. D. Shannon, *Acta Cryst*, 1976, **32**, 751–767.
- 35 D. H. Lee, J. Xu and Y. S. Meng, *Phys. Chem. Chem. Phys.*, 2013, **15**, 3304–3312.
- 36 Y. Li, Z. Yang, S. Xu, L. Mu, L. Gu, Y. Hu, H. Li and L. Chen, *Adv. Sci.*, 2015, **2**, 1500031.
- 37 L. Wang, Y.-G. Sun, L.-L. Hu, J.-Y. Piao, J. Guo, A. Manthiram, J. Ma and A.-M. Cao, *J. Mater. Chem. A*, 2017, **5**, 8752–8761.
- 38 L. Mu, S. Xu, Y. Li, Y. S. Hu, H. Li, L. Chen and X. Huang, *Adv. Mater.*, 2015, **27**, 6928–6933.
- 39 K. W. Nam, S. Kim, E. Yang, Y. Jung, E. Levi, D. Aurbach and J. W. Choi, *Chem. Mater.*, 2015, **27**, 3721–3725.
- 40 A. J. Bard and L. R. Faulkner, *Electrochemical Methods: Fundamentals and Applications*, John Wiley & Sons, Inc., Hoboken, NJ, 2nd edn., 2001.
- 41 Y. Wang, J.-Y. Lou, W. Wu, C.-X. Wang and Y.-Y. Xia, *J. Electrochem. Soc.*, 2007, **154**, A228–A234.
- 42 D. Yuan, X. Hu, J. Qian, F. Pei, F. Wu, R. Mao, X. Ai, H. Yang and Y. Cao, *Electrochim. Acta*, 2014, **116**, 300–305.
- 43 L. G. Chagas, D. Buchholz, C. Vaalma, L. Wu and S. Passerini, *J. Mater. Chem. A*, 2014, **2**, 20263–20270.

- 44 E. Talaie, V. Duffort, H. L. Smith, B. Fultz and L. F. Nazar, *Energy Environ. Sci.*, 2015, **8**, 2512–2523.
- 45 B. Mortemard De Boisse, D. Carlier, M. Guignard, L. Bourgeois and C. Delmas, *Inorg. Chem.*, 2014, **53**, 11197–11205.
- 46 E. Talaie, S. Y. Kim, N. Chen and L. F. Nazar, *Chem. Mater.*, 2017, **29**, 6684–6697.
- 47 L. Liu, X. Li, S. H. Bo, Y. Wang, H. Chen, N. Twu, D. Wu and G. Ceder, *Adv. Energy Mater.*, 2015, **5**, 1500944.



P2-type sodium transition metal oxides undergo water-driven structural changes that strongly affect electrochemical charge storage in aqueous electrolytes.